Article

Combined Experimental and DFT-TDDFT Computational Study of Photoelectrochemical Cell Ruthenium Sensitizers

Mohammad K. Nazeeruddin, Filippo De Angelis, Simona Fantacci, Annabella Selloni, Guido Viscardi, Paul Liska, Seigo Ito, Bessho Takeru, and Michael Grtzel

J. Am. Chem. Soc., **2005**, 127 (48), 16835-16847• DOI: 10.1021/ja052467l • Publication Date (Web): 12 November 2005

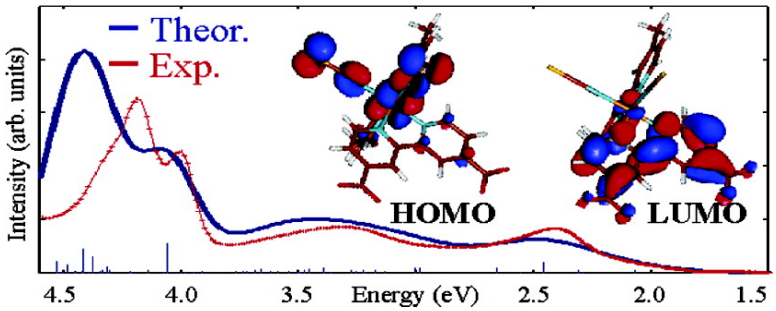

More About This Article

Additional resources and features associated with this article are available within the HTML version:

- Supporting Information
- Links to the 102 articles that cite this article, as of the time of this article download
- Access to high resolution figures
- Links to articles and content related to this article
- Copyright permission to reproduce figures and/or text from this article

View the Full Text HTML

J|A|C|S
ARTICLES
Published on Web 11/12/2005

Combined Experimental and DFT-TDDFT Computational Study of Photoelectrochemical Cell Ruthenium Sensitizers

Mohammad K. Nazeeruddin,* Filippo De Angelis,*,† Simona Fantacci,† Annabella Selloni,‡ Guido Viscardi,§ Paul Liska, Seigo Ito, Bessho Takeru, and Michael Grätzel

Contribution from the Laboratory for Photonics and Interfaces, Institute of Chemical Sciences and Engineering, School of basic Sciences, Swiss Federal Institute of Technology, CH - 1015 Lausanne, Switzerland, and Istituto CNR di Scienze e Tecnologie Molecolari (ISTM-CNR), c/o Dipartimento di Chimica, Università di Perugia, via Elce di Sotto 8, I-06123, Perugia, Italy

Received April 15, 2005; E-mail: mdkhaja.nazeeruddin@epfl.ch; filippo@thch.unipg.it

Abstract: We report a combined experimental and computational study of several ruthenium(II) sensitizers originated from the $[Ru(dcbpyH_2)_2(NCS)_2]$, N3, and $[Ru(dcbpyH_2)(tdbpy)(NCS)_2]$, N621, ($dcbpyH_2$ = 4,4′-dicarboxy-2,2′-bipyridine, tdbpy = 4,4′-tridecyl-2,2′-bipyridine) complexes. A purification procedure was developed to obtain pure N-bonded isomers of both types of sensitizers. The photovoltaic data of the purified N3 and N621 sensitizers adsorbed on TiO_2 films in their monoprotonated and diprotonated state, exhibited remarkable power conversion efficiency at 1 sun, 11.18 and 9.57%, respectively. An extensive Density Functional Theory (DFT)−Time Dependent DFT study of these sensitizers in solution was performed, investigating the effect of protonation of the terminal carboxylic groups and of the counterions on the electronic structure and optical properties of the dyes. The calculated absorption spectra are in good agreement with the experiment, thus allowing a detailed assignment of the UV−vis spectral features of the two types of dyes. The computed alignments of the molecular orbitals of the different complexes with the band edges of a model TiO_2 nanoparticle provide additional insights into the electronic factors governing the efficiency of dye-sensitized solar cell devices.

1. Introduction

Dye sensitized solar cells are currently attracting widespread academic and commercial interest for the conversion of sunlight into electricity because of their low cost and high efficiency.[1−23] In these cells, undoubtedly, the dyes and the mesoporous TiO_2 films represent the key components for high power conversion efficiencies. It was the extraordinary performance of the *cis*-dithiocyanato bis(2,2′-bipyridine-4,4′-dicarboxylate)ruthenium-(II) sensitizer (N3) attached to nanocrystalline TiO_2 films that brought a significant advance in dye sensitized solar cell technology.[24]

The sensitizer, adsorbed on the TiO_2 surface, absorbs a photon to produce an excited state, which transfers efficiently one electron onto the TiO_2 conduction band. The oxidized dye is

† Istituto CNR di Scienze e Tecnologie Molecolari (ISTM-CNR), c/o Dipartimento di Chimica, Università di Perugia, I-06123, Perugia, Italy.
‡ Department of Chemistry, Princeton University, Princeton, NJ 08540.
§ Dipartimento di Chimica Generale ed Organica Applicata, Center for Nanostructured Surfaces and Interfaces, Università di Torino, Corso Massimo D'Azeglio, 48, 10125 Torino, Italy.

(1) Grätzel, M. *Nature* **2001**, *414*, 338−344.
(2) *Special Issue: Michael Grätzel Festschrift, A Tribute for his 60th Birthday: Dye Sensitized Solar Cells.*; Nazeeruddin, M. K., Ed.; Elsevier: Amsterdam, 2004; Vol. 248.
(3) Asbury, J. B.; Ellingson, R. J.; Gosh, H. N.; Ferrere, S.; Notzig, A. J.; Lian, T. *J. Phys. Chem. B* **1999**, *103*, 3110−3119.
(4) Park, N.-G.; Kang, M. G.; Kim, K. M.; Ryu, K. S.; Chang, S. H.; Kim, D.-K.; Van de Lagemaat, J.; Benkstein, K. D.; Frank, A. J. *Langmuir* **2004**, *20*, 4246−4253.
(5) Heimer, T. A.; Heilweil, E. J.; Bignozzi, C. A.; Meyer, G. J. *J. Phys. Chem. A* **2000**, *104*, 4256−4262.
(6) Lee, J.-J.; Coia, G. M.; Lewis, N. S. *J. Phys. Chem. B* **2004**, *108*, 5269−5281.
(7) Saito, Y.; Fukuri, N.; Senadeera, R.; Kitamura, T.; Wada, Y.; Yanagida, S. *Electrochem. Comm.* **2004**, *6*, 71−74.
(8) Kamat, P. V.; Haria, M.; Hotchandani, S. *J. Phys. Chem. B* **2004**, *108*, 5166−5170.
(9) Qiu, F. L.; Fisher, A. C.; Walker, A. B.; Petecr, L. M. *Electrochem. Comm.* **2003**, *5*, 711−716.
(10) Nazeeruddin, M. K.; Humphry-Baker, R.; Liska, P.; Grätzel, M. *J. Phys. Chem. B* **2003**, *127*, 8981−8987.
(11) Adachi, M.; Murata, Y.; Takao, J.; Jiu, J.; Sakamoto, M.; Wang, F. *J. Am. Chem. Soc.* **2004**, *126*, 14943−14949.
(12) Argazzi, R.; Larramona, G.; Contado, C.; Bignozzi, C. A. *J. Photochem. Photobiol. A: Chem.* **2004**, *164*, 15−21.
(13) Bisquert, J.; Cahen, D.; Hodes, G.; Ruehle, S.; Zaban, A. *J. Phys. Chem. B* **2004**, *108*, 8106−8118.
(14) Cao, J.; Sun, J.-Z.; Hong, J.; Yang, X.-G.; Chen, H.-Z.; Wang, M. *Appl. Phys. Lett.* **2003**, *83*, 1896−1898.
(15) Durr, M.; Bamedi, A.; Yasuda, A.; Nelles, G. *Appl. Phys. Lett.* **2004**, *84*, 3397−3399.
(16) Fabregat-Santiago, F.; Garcia-Canadas, J.; Palomares, E.; Clifford, J. N.; Haque, S. A.; Durrant, J. R.; Garcia-Belmonte, G.; Bisquert, J. *J. Appl. Phys.* **2004**, *96*, 6903−6907.
(17) Figgemeier, E.; Hagfeldt, A. *Int. J. Photoenergy* **2004**, *6*, 127−140.
(18) Furube, A.; Katoh, R.; Yoshihara, T.; Hara, K.; Murata, S.; Arakawa, H.; Tachiya, M. *J. Phys. Chem. B* **2004**, *108*, 12588−12592.
(19) Hongwei, H.; Xingzhong, Z.; Jian, L. *J. Electrochem. Soc.* **2005**, *1*, 152.
(20) Kim, J. H.; Kang, M.-S.; Kim, Y. J.; Won, J.; Park, N.-G.; Kang, Y. S. *Chem. Commun.* **2004**, 1662−1663.
(21) Miyasaka, T.; Kijitori, Y. *J. Electrochem. Soc.* **2004**, *151*, A1767−A1773.
(22) Nazeeruddin, M. K.; Humphry-Baker, R.; Officer, D. L.; Campbell, W. M.; Burrell, A. K.; Grätzel, M. *Langmuir* **2004**, *20*, 6514−6517.
(23) Xue, B.; Wang, H.; Hu, Y.; Li, H.; Wang, Z.; Meng, Q.; Huang, X.; Sato, O.; Chen, L.; Fujishima, A. *Photochem. Photobiol. Sci.* **2004**, *3*, 918−919.
(24) Nazeeruddin, M. K.; Kay, A.; Rodicio, I.; Humphry-Baker, R.; Muller, E.; Liska, P.; Vlachopoulos, N.; Grätzel, M. *J. Am. Chem. Soc.* **1993**, *115*, 6382−6390.

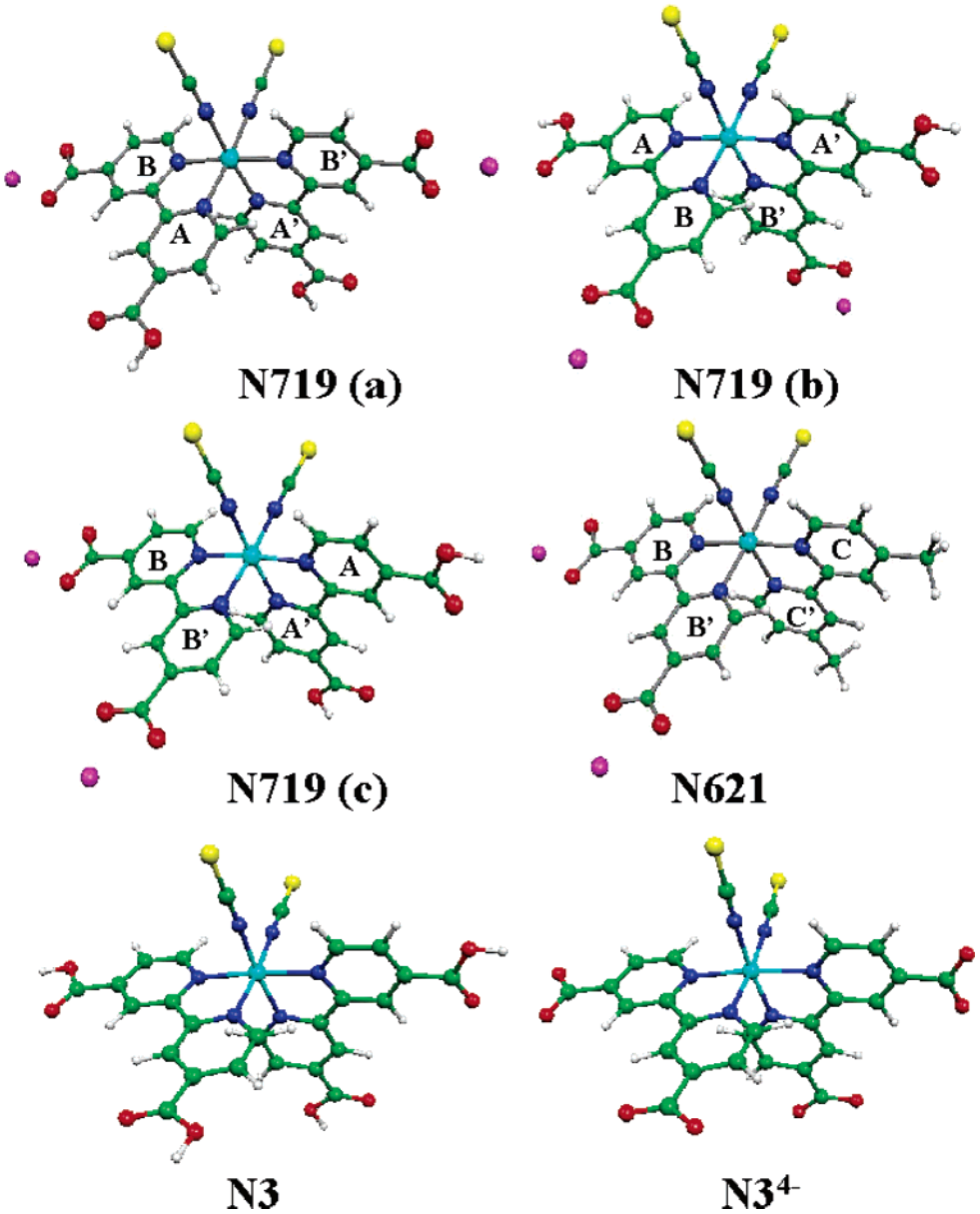

Figure 1. Optimized molecular structures of the N719 (**a**−**c** isomers), N621 and of the fully protonated and fully deprotonated N3 complexes. For the N621 complex, the 4,4′-tridecyl groups have been replaced by 4,4′-methyl groups. For all the dyes, the labels A−A′ denote the pyridines substituted in para position by protonated carboxylic groups, the labels B−B′ denote the pyridines substituted in para position by deprotonated carboxylic groups and, for the N621-derived dyes, the labels C−C ‘denote the pyridines substituted in para position by alkyl groups. Light blue = Ru; yellow = S; purple = Na; red = O; blue = N; green = C; white = H atoms.

subsequently reduced by electron donation from an electrolyte containing the iodide/triiodide redox system. The injected electron flows through the semiconductor network to arrive at the back contact and then through the external load to the counter electrode (platinum sputtered conducting glass). At the counter electrode, reduction of triiodide in turn regenerates iodide, which completes the circuit. To achieve high quantum yields of the excited state electron transfer process the dye ideally needs to be in intimate contact with the semiconductor surface. The charge separation has become controlled by irreversible chemical charge transfer kinetics, and the injected electrons from the sensitizer can, even in absence of a major electrical field, be efficiently collected and may diffuse toward the front contact of a solar cell.

The high performance achieved by N3-sensitized TiO_2 solar cell devices can be related to several factors, such as the dye broad range of visible light absorption, its relatively long-lived excited states with energies almost matching those of TiO_2 conduction band and its high thermal stability.[25] Moreover, the presence of terminal acidic carboxylic groups allows stable anchoring of the sensitizer to the semiconductor surface, so as to ensure a high electronic coupling between the dye and the semiconductor which is required for efficient charge injection. It is therefore important to analyze in detail the electronic structure of the sensitizer, to investigate the energy and composition of its excited states and their localization at the dye-semiconductor interface.

The overall conversion efficiency (η) of the dye sensitized solar cell is determined by the photocurrent density (i_{ph}), the

(25) Amirnasr, M.; Nazeeruddin, M. K.; Grätzel, M. *Thermochim. Acta* **2000**, *348*, 105−114.

open circuit potential (V_{oc}), the fill factor (ff) of the cell, and the intensity of the incident light (I_s), namely[24]

$$\eta_{global} = i_{ph}\, V_{oc}\, ff/I_s$$

In the case of a sensitizer that contains protonated carboxylic groups, upon adsorption the anchoring groups transfer most of their protons to the TiO_2 surface charging it positively, and thereby the Fermi level moves down (positively).[26−28] The electric field associated with the surface dipole generated in this way enhances the adsorption of the ruthenium complex and assists electron injection from the excited state of the sensitizer into the TiO_2 conduction band, favoring higher photocurrents. However, the positive shift of the Fermi level decreases the gap between the redox couple iodide/triiodide and the Fermi level, resulting in a lower open-circuit potential.[13] On the other hand, adsorption of a sensitizer that contains no protons moves the Fermi level negatively, leading to a higher value for the open-circuit potential while the value of the short circuit current is low.[10] Therefore, there should be an optimal degree of protonation of the sensitizer, for which the product of short circuit photocurrent and open circuit potential is high, so as to maximize the power conversion efficiency of the cell. Varying the degree of protonation of the sensitizer, however, introduces changes also in its electronic structure, so that it is important to investigate how the energy and composition of the excited states change as a function of the protonation of the terminal carboxylic groups.

In this paper, we report a combined theoretical and experimental effort aimed at providing a better understanding of the role of the sensitizer, particularly of its electronic structure and excited-state properties, in the efficiency of dye-sensitized solar cell devices. In particular, we investigate several ruthenium(II) sensitizers originated from the prototype $[Ru(dcbpyH_2)_2(NCS)_2]$, N3, dye and from the amphiphilic heteroleptic $[Ru(dcbpyH_2)(tdbpy)(NCS)_2]$, N621, dye ($dcbpyH_2$ = 4,4′-dicarboxy-2,2′-bipyridine, tdbpy = 4,4′-tridecyl-2,2′-bipyridine), in which one of the $dcbpyH_2$ ligands is substituted by a tdbpy ligand,[30a] bearing aliphatic substituents in the bipyridine para positions, see Figure 1. Amphiphilic heteroleptic sensitizers are attracting considerable interest owing to their improved stability toward water-induced desorption from TiO_2.[30]

On the experimental side, we consider the N621 dye and the N3-derived $(Bu_4N)_2[Ru(dcbpyH)_2(NCS)_2]$, N719, dye. A purification procedure was developed to obtain pure N-bonded isomers of both types of sensitizers. The photovoltaic properties of the purified N719 and N621 sensitizers have been investigated as a function of the degree of protonation of the anchoring carboxylic groups, considering both diprotonated and monoprotonated dyes.

We have carried out Density Functional Theory (DFT) and Time Dependent DFT (TDDFT) calculations in solution of the geometry, electronic structure and optical absorption spectra of a series of 13 and 7 sensitizers derived from the N3 and N621 dyes, respectively, and compared the theoretical results to those of electrochemical and spectroscopic studies obtained within the present investigation. In particular, we have extensively investigated the effect of protonation of the terminal carboxylic groups and of the presence of counterions on the electronic structure and optical properties of the two types of dyes. We finally analyzed the lineup of the molecular energy levels for the various dyes investigated in this study with the semiconductor band edges of a model TiO_2 nanoparticle. From this joint theoretical and experimental approach, significant insights into the nature of the excited states involved in the electron injection process and the role of dye protonation on the solar cell device performance are obtained.

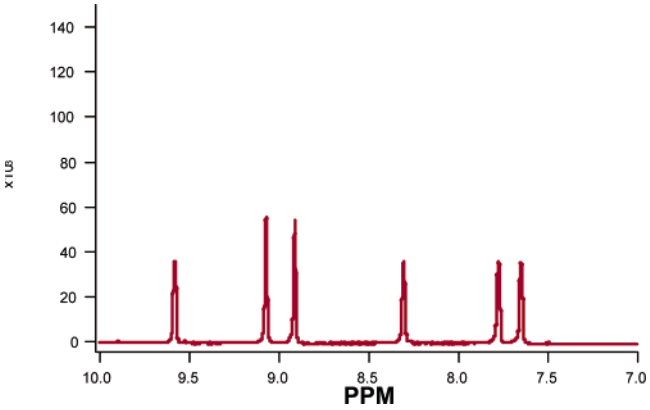

Figure 2. Part of 600 MHz proton NMR spectrum of the N719 complex in CD_3OD. For clarity the peaks in the aliphatic region are not included.

2. Experimental Section

2.1. Spectroscopic and Electrochemical Studies. Thiocyanate is an ambidentate ligand that can coordinate to the ruthenium center through the −N or −S end, and produces a mixture of isomers. The proton NMR spectra of the crude complex show peaks at lower field, which are due to S-bonded linkage isomer. Synthetic efforts on sensitizers focus on elimination of the S-bonded isomer by repeated purification on a Sephadex LH-20 column (see the Supporting Information for details on the experimental setup). Figure 2 shows the ^1H NMR spectra of the N719 complex measured in CD_3OD after three times purification.

It is striking to note the absence of linkage isomers in the N719 complex because of repeated purification and isolation at pH 4.3. The presence of six peaks in the aromatic region corresponding to two different pyridyl rings in which two pyridine rings are trans to the NCS ligands and the remaining two are trans to each other clearly show that the complex is pure N-bonded isomer. The ^{13}C NMR and ATR-FTIR data are consistent with the presence of only N-bonded isomer. The resonance peaks in the aliphatic region for N719 complex (not shown in Figure 2) are due to tetrabutylammonium cations. The integrated ratio of the aliphatic to aromatic protons shows the presence of two tetrabutylammonium cations.

The ^1H NMR spectra of the N621 complex show the presence of 12 peaks in the aromatic region corresponding to four different pyridyl rings in which all pyridine ring protons are chemically in different environment. The absence of linkage isomers in purified N621 complex is evident from the NMR spectra (not shown). A new development for dyes applied to solar cell comes from the molecular engineering of sensitizers that enhance the charge separation at the oxide solution interface.[28,29] The amphiphilic heteroleptic sensitizer N621 has several advantages compared to the N719 complex: (a) The decreased charge

(26) Nozik, A. J. *Annu. Rev. Phys. Chem.* **1978**, *29*, 189−222.
(27) Yan, S. G.; Hupp, J. T. *J. Phys. Chem.* **1996**, *100*, 6867−6870.
(28) Gerisher, H. *Electrochim. Acta* **1989**, *34*, 1005−1009.
(29) Nazeeruddin, M. K.; Pe'chy, P.; Renouard, T.; Zakeeruddin, S. M.; Humphry-Baker, R.; Comte, P.; Liska, P.; Le, C.; Costa, E.; Shklover, V.; Spiccia, L.; Deacon, G. B.; Bignozzi, C. A.; Grätzel, M. *J. Am. Chem. Soc.* **2001**, *123*, 1613−1624.
(30) (a) Nazeeruddin Md. K, Zakeeruddin S. M., Lagref J−J., Barolo C., Viscardi G., Liska P., Comte P., Schenk K.; Grätzel M. *Coord. Chem. Rev.* **2004**, *248*, 1317−1328. (b) Zakeeruddin, S. M.; Nazeeruddin, M. K.; Humphry-Baker, R.; Pechy, P.; Quagliotto, P.; Barolo, C.; Viscardi, G.; Grätzel, M. *Langmuir* **2002**, *18*, 952−954.

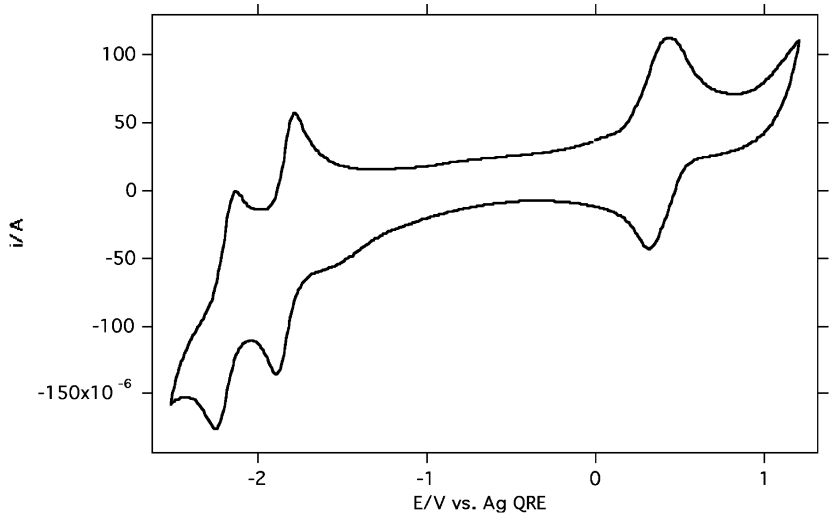

Figure 3. Cyclic voltammogram of N621 complex measured in DMF solution containing 0.1 M TBA(PF_6) using a gold electrode with scan speed of 500 mV/s.

on the sensitizer attenuates the electrostatic repulsion and thereby increasing the dye loading. (b) The presence of hydrophobic moiety on the ligand increases the stability of solar cells toward water induced desorption. (c) The oxidation potential of these complexes is cathodically shifted compared to the N3 sensitizer, which increases the reversibility of ruthenium III/II couple leading to enhanced stability.[31]

Upon scanning to positive potentials a reversible couple at $E_{1/2} =$ 0.35 V vs Fc with a separation of 0.1 V between anodic to cathodic peak was observed due to the $Ru^{II/III}$ couple. The ruthenium oxidation potential in the N621 complex is shifted cathodically by 0.15 V, compared to the N719 oxidation potential, which is observed at $E_{ox} =$ 0.5 V vs Fc as an irreversible wave. The difference (0.15 V) in the oxidation potential of N621 complex compared to that of N719 is due to the donor influence of 4,4′-tridecyl-2,2′-bipyridine to the ruthenium center.

For the N621 complex, when scanning toward negative potentials two reversible waves were observed at $E_{1/2} = -1.83$ and -2.17 V vs Fc, which are assigned to the reduction of 4,4′-dicarboxylic acid-2,2′-bipyridine and 4,4′-tridecyl-2,2′-bipyridine ligand, respectively (Figure 3). The separation between the anodic and the cathodic peaks of couples is 0.1 V. The N719 complex shows reduction potential at $E_{1/2} = -1.79$ V vs Fc and is assigned to the reduction of 4,4′-dicarboxylic acid-2,2′-bipyridine ligand. A detailed description of the electronic structure and optical absorption spectra of the two complexes is reported in the theoretical section, see below.

2.2. Photovoltaic Data. Figure 4 shows the photocurrent action spectrum of N621 solar cells based on a swift self-assembled procedure on double layers of 12 + 4 μm thick nanocrystalline TiO_2 films. The incident monochromatic photon-to-current conversion efficiency (IPCE) plotted as a function of excitation wavelength reaches a value of 85% in the plateau region. The important effect of the 4-μm thick 400-nm particles layer is obvious in the red region. The incident monochromatic photon-to-current conversion efficiency value at 700 nm is twice as high for the TiO_2 film containing a scattering layer as compared to the 12 μm thick TiO_2 film without scattering layer. From the overlap integral of this curve, one measures a short circuit photocurrent density of 16 mA/cm^2. In agreement with this measurement under a standard global AM 1.5 solar conditions the cell gave a photocurrent density of 16.8 mA/cm^2, 778 mV open circuit potential and 0.73 fill factor yielding power conversion efficiencies of 9.57%.

The structural features of the dye should match the requirements for current rectification: in analogy to the photofield effect in transistors,

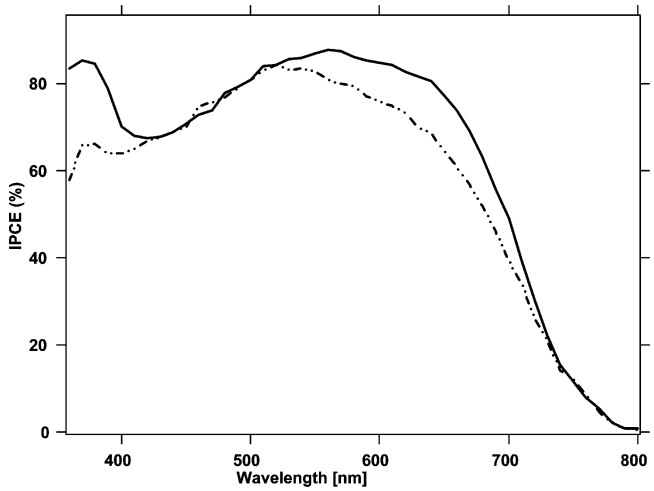

Figure 4. Photocurrent action spectra obtained with the N621 (dashed line) and N719 (solid line) sensitizers attached to nanocrystalline TiO_2 film. The incident photon to current conversion efficiency is plotted as a function of the wavelength.

the gate for unidirectional electron flow from the electrolyte through the junction and into the oxide is opened by the photoexcitation of the sensitizer. The reverse charge flow, i.e., recapture of the electron by the oxidized redox couple in the electrolyte is impaired by judicious design of the sensitizer having alkyl chains 4,4′-tridecyl-2,2′-bipyridine. The latter should form a tightly packed insulating monolayer blocking the dark current. As mentioned above, we have obtained 9.57% power conversion efficiency with N621 dye using a swift deposition procedure. Under similar conditions at 1 sun, the N719 sensitized cell gave a photocurrent density of 17.6 mA/cm^2, 800 mV open circuit potential and 0.73 fill factor yielding power conversion efficiencies of 10.26%. Table 1 illustrates the effect of dye deposition solvent and the dye dipping time on the photovoltaic performance of the cell. The data in the Table 1 show that the optimum dipping time for concentrated solutions is 10−15 min. The longer and the shorter dipping times resulted in lower efficiency compared to the 10−15 min. The influence of dye deposition solvent on current and voltage was investigated in *N*,*N*-dimethylformamide, and methoxypropionitrile solvents. The optimum performance of dye-sensitized solar cell was observed with methoxypropionitrile solvent as dye deposition medium. The rapid deposition method of concentrated solution is potentially useful for fabricating dye-sensitized solar cells online at room temperature by screen-printing or inkjet printing.

(31) Wang, P.; Zakeeruddin, S. M.; Moser, J.; Nazeeruddin, M. K.; Sekiguchi, T.; Grätzel, M. *Nat. Mater.* **2003**, *2*, 402−407.

Table 1. Performance Characteristics of Photovoltaic Cells Based on Nanocrystalline TiO_2 Films Sensitized by N621 and N719 Dye in *N,N*− Dimethylformamide (DMF) and Methoxypropionitrile (MPN)

dye	dipping time (min)	concentration (M)	solvent	Isc (mA/cm^2)	Voc (mV)	fill factor	efficiency at 1 Sun (η %)
N719	5	2×10^{-2}	MPN	16.55 ± 0.1	791 ± 5	0.71	9.5 ± 0.2
N719	10	2×10^{-2}	MPN	17.5 ± 0.1	800 ± 5	0.73	10.25 ± 0.2
N719	15	2×10^{-2}	MPN	17.6 ± 0.1	799 ± 5	0.73	10.29 ± 0.2
N719	20	2×10^{-2}	MPN	17.8 ± 0.1	789 ± 5	0.71	9.97 ± 0.2
N719	30	2×10^{-2}	MPN	17.89 ± 0.1	789 ± 5	0.69	9.74 ± 0.2
N719	35	2×10^{-2}	MPN	17.29 ± 0.1	783 ± 5	0.72	9.83 ± 0.2
N719	10	2×10^{-2}	DMF	18.28 ± 0.1	772 ± 5	0.72	10.22 ± 0.2
N719	1200	5×10^{-4}	1:1[a]	17.73 ± 0.5	846 ± 20	0.75	11.18
N621	1200	3×10^{-4}	1:1[a]	15.85 ± 0.1	762 ± 5	0.73	8.81
N621	10	18×10^{-3}	MPN	16.81 ± 0.1	777 ± 5	0.73	9.57
N621	10	18×10^{-3}	DMF	15.94 ± 0.1	789 ± 5	0.73	9.16

[a] The dye solutions were prepared in 1:1 CH_3CN+ *tert*-BuOH solution mixture and was added 1 equivalent of tetrabutylammonium chenodeoxycholic acid salt to generate monoprotonated species. The data were collected using A6141 electrolyte.

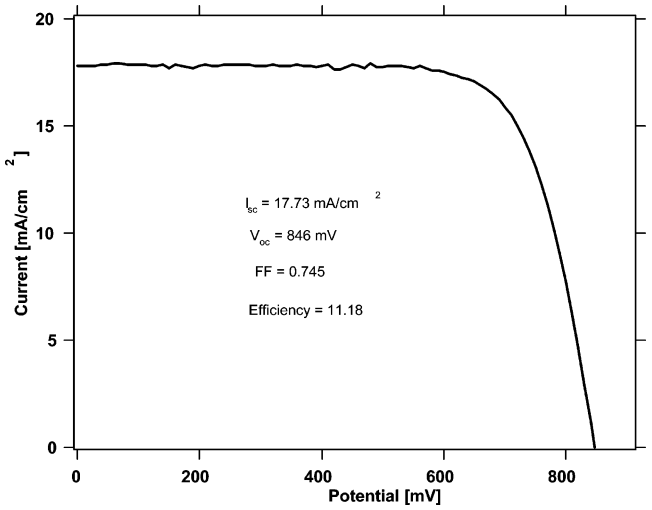

Figure 5. Photocurrent−voltage curve of a solar cell based on an electrolyte containing guanidinium thiocyanate as self-assembly facilitating agent. The N719 sensitizer was passed three times over a Sephadex LH-20 column for purification. The cell was equipped with an antireflecting coating. The conversion efficiency in full AM 1.5 sunlight illumination (100 mW cm^{-2}) is reported. The cell is masked with black plastic to avoid the diffusive light leaving an active cell area of 0.158 cm^2.

The N621 and N719 dye solutions containing the monoprotonated species were also prepared in 1:1 CH_3CN + *tert*-BuOH solution mixture by adding 1 equiv of tetrabutylammonium chenodeoxycholic acid salt to the dye solution. The concentration of the dye solution was typically between 3 and 5×10^{-4} M and the electrodes were dipped for 18−20 h. Figure 5 shows the current−voltage characteristics obtained with a sandwich cell under illumination by simulated AM 1.5 solar light using N719 dye.

The photocurrent action spectra of the N719 sensitizer show broad features covering a large part of the visible spectrum, see Figure 4. The incident monochromatic photon-to-current conversion efficiency (IPCE) plotted as a function of excitation wavelength exhibits in the plateau region a value of 87%. At one sun the monoprotonated N719 sensitized solar cell exhibited 17.73 ± 0.5 mA current, 846 mV potential and fill factor 0.75 yielding an overall conversion efficiency of 11.18%. This efficiency is a remarkable improvement compared to our previous data using the N719 complex that contains two protons. The cell voltage is mainly responsible for increased efficiency. Under similar conditions, the N621 sensitized solar cell showed slightly lower efficiency compared to the swift deposition procedure (see Table 1).

3. Theoretical Section

3.1. Models and Computational Details. We have investigated all of the possible complexes derived from the N3 dye corresponding to 4, 2, 1, and 0 protons on the carboxylic groups, considering both the anionic complexes and saturating the negative charge by counterions; for the di- and monoprotonated complexes we also considered the various (three and two, respectively) possible isomers, resulting in a total of 13 N3-derived dyes. For the N621-derived dyes the species with 2, 1, and 0 protons have been investigated, including the counterions effect and the possible isomers, for a total of 7 N621-derived dyes. For computational convenience, we mimic the experimental bulky tetrabutylammonium counterions by Na^+ ions. We generally refer to the N3-derived species as $[N3(x\mathrm{H}-y\mathrm{Na})]^{(x+y-4)}$, where x is the number of protons, y is the number of sodium counterions, and the total charge of the molecule is $(x+y-4)$. For the N621-derived dyes, the bulky tridecyl groups in para to one of the bipyridine ligands have been modeled by smaller methyl groups. We analogously refer to the various N621-derived dyes as $[N621(x\mathrm{H}-y\mathrm{Na})]^{(x+y-2)}$. Notice that within the model simplifications adopted in the calculations, $[N3(2\mathrm{H}-2\mathrm{Na})]^{(0)}$ and $[N3(1\mathrm{H}-3\mathrm{Na})]^{(0)}$ correspond to the experimentally characterized diprotonated and monoprotonated N719 species, while $[N3(4\mathrm{H}-0\mathrm{Na})]^{(0)}$ corresponds exactly to the N3 sensitizer. Similarly, $[N621(2\mathrm{H}-0\mathrm{Na})]^{(0)}$, $[N621(1\mathrm{H}-1\mathrm{Na})]^{(0)}$, $[N621(0\mathrm{H}-2\mathrm{Na})]^{(0)}$ represent the models of the experimentally characterized diprotonated, monoprotonated, and nonprotonated N621 species.

Calculations have been performed using the B3LYP exchange-correlations functional,[32] as implemented in the Gaussian03 program package.[33] Geometry optimizations were performed in water solution using a 3-21 g* basis set[34] without any symmetry constraints. Solvation effects were included by means of the conductor-like polarizable continuum model (C−PCM).[35] For $[N3(2\mathrm{H}-2\mathrm{Na})]^{(0)}$, corresponding to the diprotonated N719 dye, and for the related anionic $[N3(2\mathrm{H}-0\mathrm{Na})]^{(2-)}$ species, we optimized the geometries of the three possible diprotonated complexes (with the two protonated carboxylic groups trans−trans, cis−cis and cis−trans to the NCS ligands) which we label as **a**, **b**, and **c**, see Figure 1. Also, for $[N3(1\mathrm{H}-3\mathrm{Na})]^{(0)}$, corresponding to the monoprotonated N719 dye, and for the analogous anionic $[N3(1\mathrm{H}-0\mathrm{Na})]^{(3-)}$ species, as well as for $[N621(1\mathrm{H}-1\mathrm{Na})]^{(0)}$, corresponding to the monoprotonated N621

(32) Becke, A. D. *J. Chem. Phys.* **1993**, *98*, 5648−5652.
(33) Frisch, M. J., et al. *Gaussian 03*, revision B.05; Gaussian, Inc.: Pittsburgh, PA, 2003 (Supporting Information Available for complete ref 33).
(34) Binkley, J. S.; Pople, J. A.; Hehre, W. J. *J. Am. Chem. Soc.* **1980**, *102*, 2, 939−947.
(35) (a) Barone, V.; Cossi, M. *J. Phys. Chem. A* **1998**, *102*, 1995−2001. (b) Cossi, M.; Rega, N.; Scalmani, G.; Barone, V. *J. Comput. Chem.* **2003**, *24*, 669−681.

Table 2. Main Optimized Geometrical Parameters (Å, deg) for the $[N3(4H-0Na)]^{(0)}$, I, **a**−**c** Isomers of $[N3(2H-2Na)]^{(0)}$, II-IV, $[N621(2H-0Na)]^{(0)}$, V, and $[N621(0H-2Na)]^{(0)}$, VI, Compared to Available X-ray Data for the N3 Complex,[43] Corresponding to $[N3(4H-0Na)]^{(0)}$[a]

parameter	exp. (N3)	I	II	III	IV	V	VI
Ru−NCS	2.048(12)−2.046(16)	2.072−2.072	2.079−2.079	2.081−2.082	2.082−2.081	2.082−2.083	2.083−2.083
$Ru-bpy_{cis}$	2.036(15)−2.058(12)	2.078−2.078	2.092−2.092	2.086−2.085	2.093−2.084	2.083−2.097	2.088−2.096
$Ru-bpy_{trans}$	2.030(13)−2.013(14)	2.068−2.069	2.073−2.073	2.080−2.080	2.081−2.070	2.068−2.085	2.076−2.082
N−C(NCS)	1.162(21)−1.103(27)	1.184−1.184	1.181−1.181	1.181−1.181	1.181−1.181	1.181−1.181	1.181−1.181
C−S(NCS)	1.615(18)−1.685(22)	1.638−1.638	1.647−1.647	1.648−1.648	1.647−1.648	1.648−1.648	1.650−1.650
$<N(NCS)-Ru-N(NCS)'$	88.7(5)	90.7	89.3	90.4	90.5	91.0	91.2
$<N(bpy_{trans})-Ru-N(bpy_{cis})$	79.5(5)	78.9−78.9	78.9-78.9	78.9-78.9	78.9-79.0	79.0-78.5	78.9-78.5
$<N(bpy_{trans})-Ru\ N(bpy_{trans})$	90.6(5)	92.2	92.3	91.6	91.7	91.7	91.5
$<N(bpy_{cis})-Ru-N(bpy_{cis})$	174.5(6)	175.3	175.4	175.6	175.2	175.2	174.9

[a] The subscripts cis and trans refer to the SCN ligands. For the asymmetric c $[N3(2H-2Na)]^{(0)}$ isomer (IV) the first entries correspond to parameters referring to atoms which belong to groups trans to, or belonging to the bipyridine bearing the COO^-Na^+ groups. For $[N621(2H-0Na)]^{(0)}$, V, and $[N621(0H-2Na)]^{(0)}$, VI, the first and second entry correspond to parameters referring to atoms which belong to groups trans to, or belonging to the bipyridine bearing the COOH or COO^-Na^+ groups.

dye, and for the related $[N621(1H-0Na)]^{(1-)}$ charged species, we optimized the geometries of the two possible monoprotonated complexes (with the protonated carboxylic group cis and trans to the NCS ligands); these are denoted as **a′** and **b′**, respectively. TD-DFT excited states calculations of the lowest singlet−singlet and singlet−triplet excitations were performed in water solution using the same 3-21 g* basis set used for geometry optimizations, by means of the nonequilibrium version of the C−PCM algorithm.[36] We note that in the present G03 implementation dispersion-repulsion contributions to solvent shifts are not included since they are identical for different electronic states. For the simulation of the absorption spectra of the $[N3(2H-2Na)]^{(0)}$ and $[N621(0H-2Na)]^{(0)}$ species, corresponding to the experimentally characterized diprotonated N719 and nonprotonated N621 dyes, respectively, we performed TDDFT calculations using the larger DGDZVP basis set[37] in ethanol solution. In this case, the 50 (3) lowest singlet−singlet (singlet−triplet) excitation energies were computed. The simulation of the absorption spectra was performed by a convolution of Gaussian functions centered at the calculated excitation energies, with a constant $\sigma = 0.20$ eV for all the transitions. For $[N621(0H-2Na)]^{(0)}$ we also simulated the spectrum by a variable σ, using $\sigma = 0.20$ and 0.12 eV for the transitions below and above 4.0 eV, respectively, see Supporting Information.

Previous theoretical investigations on dye sensitizers were mainly performed by means of semiempirical[38] and DFT calculations,[39] and only recently TDDFT investigations on Ru(II) sensitizers have appeared in the literature.[40] In particular, we [40d−e,41] and Guillemoles, et al.[40b] have shown that inclusion of solvation effects is crucial when describing the electronic structure and absorption spectra of Ru(II)-polypyridyl complexes; relevant differences are found in the electronic structure and spectra of the tetradeprotonated N3 dye ($[N3(0H-0Na)]^{(4-)}$ in vacuo[40a] and in solution.[40e] Solvation effects have been found to be important for a correct description of dye-sensitized TiO_2 nanoparticles as well.[42] Moreover, even though a polarizable continuum model usually properly accounts for solvation effects in dye sensitizers including subtle effects such as solvatochromism,[40d] in the present case we checked the effect of explicit solvation in conjunction to C−PCM, including two water molecules solvating each carboxylate group of the anionic $[N3(0H-0Na)]^{(4-)}$ species. Notice that results reported here for the $[N3(4H-0Na)]^{(0)}$ species optimized in water solution are slightly different from those of ref 40e, in which the geometry was optimized in vacuo.

3.2. Geometries. In Table 2, main optimized geometrical parameters for a few species, namely $[N3(4H-0Na)]^{(0)}$, the **a**−**c** isomers of $[N3(2H-2Na)]^{(0)}$, $[N621(2H-0Na)]^{(0)}$, and $[N621(0H-2Na)]^{(0)}$, are compared to available X-ray data for the N3 complex[43] (we remind that the latter corresponds to the computationally investigated $[N3(4H-0Na)]^{(0)}$ species).

The agreement between crystal structure parameters and main calculated data in solution is quite good, suggesting that the geometry is only partially affected by solvation, since the general slight overestimate of the calculated bond lengths with respect to the experimental data is present also in gas-phase calculations.[40f,41a] On the other hand, bond angles are accurately reproduced by our calculations. From Table 2, it appears that the geometry of the two NCS groups is only marginally affected by the different bipyridine substituents and only the symmetric $[N3(4H-0Na)]^{(0)}$ complex and the **a** $[N3(2H-2Na)]^{(0)}$ isomer, which have protonated carboxylic groups trans to the NCS ligands, show slightly shorter Ru−N(NCS) bonds compared to the other structures (2.072 and 2.079 vs 2.082−2.083 Å). The most significant differences in geometry are found for the $Ru-N_{bpy}$ bond lengths, with the $Ru-N_{bpy}$ bonds of the bipyridine ligands bearing the aliphatic substituents in $[N621(2H-0Na)]^{(0)}$ and $[N621(0H-2Na)]^{(0)}$ being longer both in cis and trans coordination to the NCS ligands.

(36) Cossi, M.; Barone, V. *J. Chem. Phys.* **2001**, *115*, 4708−4717.
(37) Godbout, N.; Salahub, D. R.; Andezelm, J.; Wimmer, E. *Can. J. Chem.* **1992**, *70*, 560.
(38) (a) Rensmo, H.; Södergren, S.; Patthey, L.; Westmark, K.; Vayssieres, L.; Khole, O.; Brühwiler, P. A.; Hagfeldt, A.; Siegbahn, H. *Chem. Phys. Lett.* **1997**, *274*, 51−57. (b) Nazeeruddin, Md. K.; Zakeeruddin, S. M.; Humphry-Baker, R.; Goreslky, S. I.; Lever, A. B. P.; Grätzel, M. *Coord. Chem. Rev.* **2000**, *208*, 213−226. (c) Renouard, T.; Fallahpuor, R.-A., Nazeeruddin, Md. K.; Humphry-Baker, R.; Goreslky, S. I.; Lever, A. B. P.; Grätzel, M. *Inorg. Chem.* **2002**, *41*, 367−378. (d) Cecchet, F.; Gioacchini, A. M.; Marcaccio, M.; Paolucci, F.; Roffia, S.; Alebbi, M.; Bignozzi, C. A. *J. Phys. Chem. B* **2002**, *106*, 3926−3932.
(39) Daul, C.; Baerends, E. J.; Vernooijs, P. *Inorg. Chem.* **1994**, *33*, 3538−3543.
(40) (a) Monat, J. E.; Rodriguez, J. H.; McCusker, J. K. *J. Phys. Chem. A* **2002**, *106*, 7399−7406. (b) Guillemoles, J.-F.; Barone, V.; Joubert, L.; Adamo, C. *J. Phys. Chem. A* **2002**, *106*, 11354−11360. (c) Zabri, H.; Gillaizeau, I.; Bignozzi, C. A.; Caramori, S.; Charlot, M.-F.; Cano-Boquera, J.; Odobel, F. *Inorg. Chem.* **2003**, *42*, 6655−6666. (d) Fantacci, S.; De Angelis, F.; Selloni, A. *J. Am. Chem. Soc.* **2003**, *125*, 4381−4387. (e) De Angelis, F.; Fantacci, S.; Selloni, A. *Chem. Phys. Lett.* **2004**, *389*, 204−208.
(41) (a) Fantacci, S.; De Angelis, F.; Sgamellotti, A.; Re, N. *Chem. Phys. Lett.* **2004**, *396*, 43−48. (b) Fantacci, S.; De Angelis, F.; Wang, J.; Bernhard, S.; Selloni, A. *J. Am. Chem. Soc.* **2004**, *126*, 9715−9723. (c) Fantacci, S.; De Angelis, F.; Sgamellotti, A.; Marrone, A.; Re, N. *J. Am. Chem. Soc.* **2005**, *127*, 14144−14145.
(42) De Angelis., F.; Tilocca., A.; Selloni, A. *J. Am. Chem. Soc.* **2004**, *126*, 15024−15025.
(43) Shklover, V.; Ovchinnikov, Yu. E.; Graginsky, L. S.; Zakeeruddin, S. M.; Grätzel, M. *Chem. Mater.* **1998**, *10*, 2533−2541.

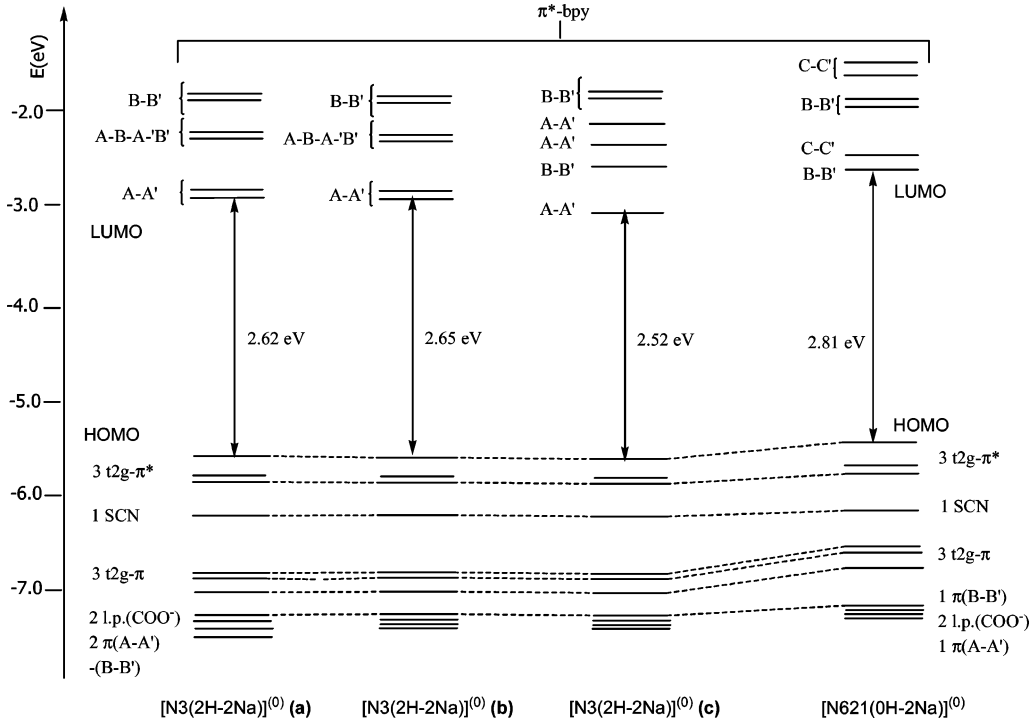

Figure 6. Comparison between the frontier orbitals of the $[N3(2H-2Na)]^{(0)}$ **a**−**c** isomers and of $[N621(0H-2Na)]^{(0)}$ models of the diprotonated N719 and nonprotonated N621 complexes, respectively. Results obtained with the DGDZVP basis set in ethanol solution are reported. Energy scale in eV.

3.3. Electronic Structure. A schematic representation of the energy levels for $[N621(0H-2Na)]^{(0)}$ and for the **a**−**c** $[N3(2H-2Na)]^{(0)}$ isomers calculated with the DGDZVP basis set in ethanol solution is reported in Figure 6.

For all of the considered complexes, the pattern of the occupied orbitals is qualitatively similar. The seven highest occupied molecular orbitals (HOMOs) can be divided into three subgroups. The almost degenerate HOMO−HOMO-2, lying within ca. 0.3 eV, have essentially ruthenium t_{2g} character (47%−53%) with sizable contribution coming from the NCS ligand orbitals, mixed in an antibonding fashion with metal states, see Figure 7. The HOMO-3, lying ca. 0.3 eV below the HOMO-2, is an isolated orbital made of a nonbonding combination of the sulfur lone pairs and the nitrogen p orbitals localized on both NCS ligands. At lower energy, ca. 0.5 eV below the HOMO-3, the HOMO-4/HOMO-6 set represents the bonding counterpart of the HOMO−HOMO-2, corresponding to the combination between the Ru− t_{2g} and the NCS π orbitals. This relevant thiocyanate character in the HOMOs was already found in the N3 dye,[38a,40e−f] and seems to play an important role in the regeneration of dye sensitized solar cells.[38a] Below the seven HOMOs, a set of four orbitals is found, corresponding to two bipyridine π bonding orbitals and two carboxylate oxygen lone pairs. As it can be noticed from Figure 6, changing the relative arrangement of the protonated/deprotonated carboxylic groups in the **a**−**c** $[N3(2H-2Na)]^{(0)}$ isomers does not lead to sizable changes in the energy and character of the occupied levels.

The lowest unoccupied molecular orbitals (LUMOs) of the investigated complexes are a set of bipyridine π^* orbitals, with different localization depending on the protonation of the terminal carboxylic groups as well as on the substituents in the bipyridine ligands. The LUMOs in Figure 6 are classified on the basis of their localization on the single pyridines, according to the labels of Figure 1. Isodensity plots of selected molecular orbitals of $[N3(2H-2Na)]^{(0)}$ (**a** isomer) and $[N621(0H-2Na)]^{(0)}$ are reported in Figure 7. For $[N3(2H-2Na)]^{(0)}$ the LUMOs appear as three couples of almost degenerate orbitals: the LUMO/LUMO+1, LUMO+2/LUMO+3, and LUMO+4/LUMO+5 couples are essentially localized over the pyridines bearing the protonated carboxylic groups (A−A′), delocalized all over the two bipyridines (A−B−A′−B′), and localized over the pyridine ligands bearing the deprotonated carboxylic groups (B−B′), respectively, see Figure 7. The stabilization of the π^* orbitals localized on the pyridine ligands bearing the protonated carboxylic groups is a common feature of all the investigated N3-derived dyes. For the $[N621(0H-2Na)]^{(0)}$ species the LUMO is mainly localized on the bipyridine bearing the carboxylates (B−B′), while the LUMO+1 is localized on the bipyridine bearing the alkyl substituents (C−C′). For both type of complexes, the A−A′ and B−B′ π^* orbitals show sizable contributions from the carboxylic groups; this should favor the electron injection from the dye excited states to the semiconductor surface. We also notice, that while the **a** and **b** isomers of $[N3(2H-2Na)]^{(0)}$ show essentially the same electronic structure, the **c** isomer shows relevant differences in the pattern of the unoccupied orbitals, which results in a reduction of the HOMO−LUMO gap. This is due to the fact that the two bipyridine ligands in the **c** isomer are no longer equivalent.

The calculated electronic structures for the $[N3(2H-2Na)]^{(0)}$ **a**−**c** and $[N621(0H-2Na)]^{(0)}$ models are consistent with the experimental cyclic voltammograms of the N719 and N621 dyes, showing an increase of the oxidation potential of 0.15 V and a slight decrease of the reduction potential of 0.04 V going from N621 to N719. For $[N621(0H-2Na)]^{(0)}$ we calculate the HOMO at −5.37 eV while for the $[N3(2H-2Na)]^{(0)}$ the HOMO is at −5.59 eV. The HOMO energy difference in the two complexes, 0.22 eV, nicely correlates with the experimental trend of oxidation potentials. Moreover, for $[N621(0H-2Na)]^{(0)}$,

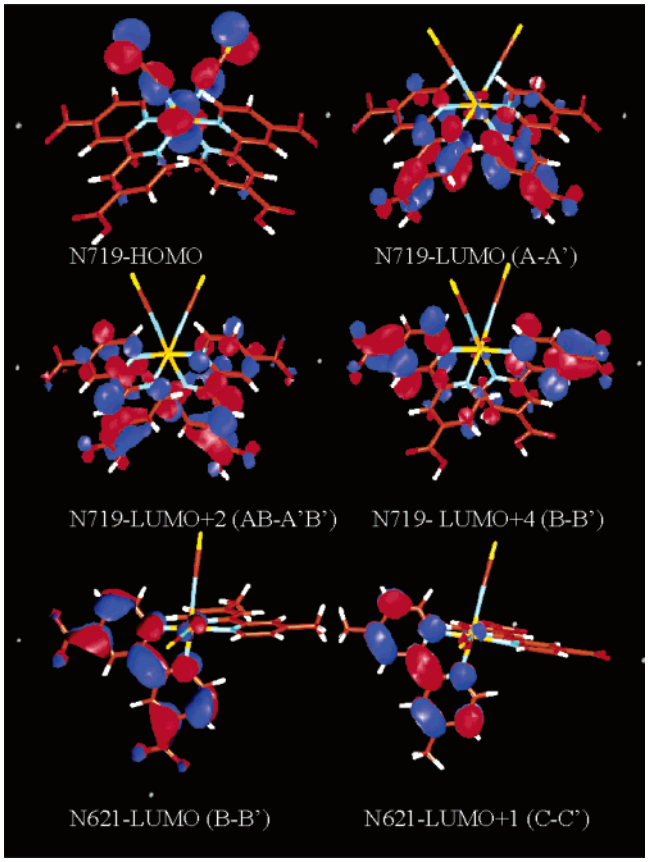

Figure 7. Isodensity plot (isodensity value = 0.035) of HOMO, LUMO, LUMO+2 and LUMO+4 of the $[N3(2H-2Na)]^{(0)}$ model (**a** isomer) of the N719 complex and of the LUMO and LUMO+1 of the $[N621(0-2Na)]^{(0)}$ model of the N621 complex. The LUMOs are classified on the basis of their localization, as defined in Figure 1. Additional orbital plots are available as Supporting Information.

the computed LUMO and LUMO+1 energies are −2.56 eV and −2.32 eV, respectively, which is consistent with the presence of two reduction potentials separated by 0.34 V in the cyclic voltammogram of N621. Thus, from the character of the LUMO and LUMO+1 in the $[N621(0H-2Na)]^{(0)}$ model, the two reduction potentials are assigned to the two π^* orbitals localized over the bipyridine ligands bearing the deprotonated carboxylic (B−B′) and aliphatic groups (C−C′), respectively.

3.4. Absorption Spectra. A comparison between the experimental and theoretical absorption spectra of the nonprotonated N621 complex in ethanol solution is reported in Figure 8. The experimental spectrum shows three main features, labeled as I, II, and III, in order of increasing energy. The two almost equally intense bands I and II, at 2.41 and 3.32 eV, are followed at higher energy by two close and intense peaks at 4.00 and 4.19 eV, forming the III feature. By comparing this experimental spectrum with the absorption spectrum of the $[N621(0H-2Na)]^{(0)}$ model calculated in ethanol solution, we notice that the agreement between theory and experiment is good both in terms of band positions and relative intensity. In particular, the computed I and II bands are at 2.49 and 3.46 eV, respectively, with band I slightly less intense than band II. The theoretical band III gives rise to a more intense feature at 4.29 eV, and appears to be composed by two groups of transitions, at ca. 4.1 and 4.4 eV. We notice that reducing the Gaussian width used for the simulation of the transitions above 4.0 eV leads to an

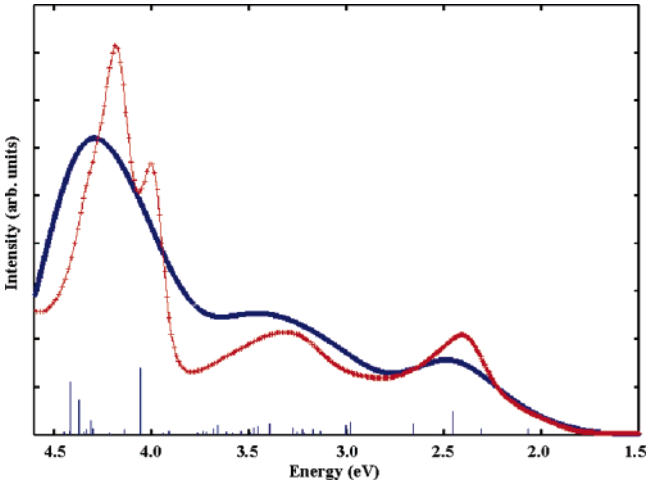

Figure 8. Comparison between calculated (blue line) and experimental (red line) spectra of the $[N621(0H-2Na)]^{(0)}$ model and of the nonprotonated N621 complex. Blue vertical lines correspond to calculated excitation energies and oscillator strengths. Energy in eV. The experimental (calculated) absorption maxima of bands I−III are at the following: 2.41 (2.49), 3.32 (3.46) and 4.00−4.19 (4.29) eV.

improved overall spectral shape, showing the band III substructure (Supporting Information).

We discuss here only the most relevant transitions constituting each band, while a detailed list of excitation energies with the relative oscillator strengths (f) is reported as Supporting Information. We compute two transitions of significant intensity below 2.7 eV, which give rise to band I. The final states of these transitions are the LUMO and LUMO+1, and the initial states are in the first set of Ru−SCN t_{2g}-π^* orbitals (HOMO−HOMO-2). Therefore we assign band I as a mixed metal-NCS to bipyridine charge transfer band. The dominating transition composing this band, at about 2.46 eV ($f = 0.097$), has as arriving state the LUMO, localized essentially on the bipyridine bearing the carboxylate groups (B−B′), while for the next most intense transition, at about 2.65 eV ($f = 0.047$), the final state is the LUMO+1, which is mainly localized on the bipyridine bearing the alkyl groups (C−C′). At lower energies, two weaker transitions give rise to the band tail. At higher energies, band II appears to be composed by a series of low-intensity transitions spanning the range 3.0−3.9 eV. For most of these transitions, the starting orbitals are both Ru−NCS sets of HOMOs and the final states involve the entire set of the first six LUMOs. Band II appears at higher energy because of the involvement of the lower set of HOMOs and higher set of LUMOs in the starting and arriving states, respectively. Interestingly, one of the transitions composing band II, namely the transition at 3.13 eV ($f = 0.012$), originates from the HOMO-3, localized on the NCS ligands, to the LUMO, and therefore constitutes a ligand (NCS) to ligand (bipyridine) charge transfer (LL′CT) transition. We also notice that a few weak d−d transitions contribute to band II. The most intense transitions composing band III are found at 4.07 ($f = 0.276$), 4.37 ($f = 0.145$), and 4.42 ($f = 0.221$) eV and give rise to the experimentally characterized sub-structure of this feature. The transition at 4.07 eV is an intraligand $\pi-\pi^*$ transition having the LUMO as arriving state, and generates therefore an excited-state localized within the bipyridine ligand which carries the deprotonated carboxylic groups (B−B′); the two transitions at 4.37 and 4.42 eV have, on the other hand, the LUMO+1 and LUMO+5 as arriving states, and generate

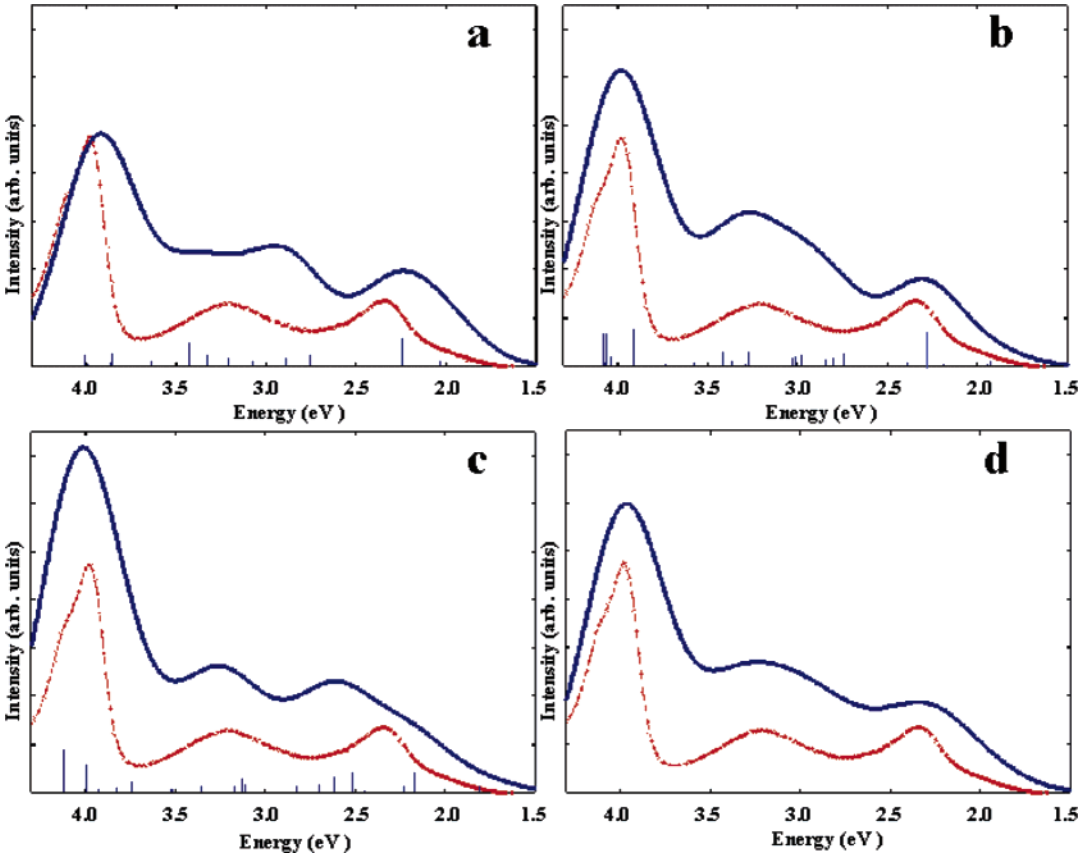

Figure 9. **a**−**c.** Comparison between the calculated (blue line) spectra of the [N3(0H-2Na)]$^{(0)}$ models (**a**−**c** isomers) and of the experimental N719 spectrum (red line) in ethanol solution. Blue vertical lines correspond to calculated excitation energies and oscillator strengths. **d.** Comparison between the average calculated spectrum (blue line) for the three **a**−**c** isomers and the experimental spectrum (red line). Energy in eV. Calculated absorption maxima of bands I−III: (**a**) 2.24, 2.96−3.37, 3.92 eV; (**b**) 2.31, 3.27, 3.98 eV; (**c**) 2.62, 3.26, 4.01 eV; (**d**) 2.30, 3.29, 3.97 eV. The experimental absorption maxima of bands I−III are at 2.35, 3.22, and 3.97 eV.

therefore excited states mainly localized within the bipyridine ligand bearing the aliphatic substituents (C−C′). Interestingly, while the transition at 4.07 eV is of pure $\pi-\pi^*$ character, the two transitions at 4.37 and 4.42 eV have also a considerable percentage of Ru−NCS orbitals in the starting states. For the [N621(0H−2Na)]$^{(0)}$ model, the lowest singlet−triplet transition is computed at 1.90 eV and corresponds essentially to a HOMO−LUMO excitation, giving therefore rise to a Ru−NCS → dcbpy excited-state localized on the bipyridine bearing the carboxylates (B−B′).The lowest triplet excited-state localized on the bipyridine bearing the alkyl substituents (C−C′) is computed as the third triplet excited state at 2.17 eV.

In Figure 9a−c, we compare the experimental spectrum of the N719 dye in ethanol solution with the calculated spectra for the **a**−**c** [N3(2H-2Na)]$^{(0)}$ isomers. The experimental absorption spectrum of the N719 complex is qualitatively similar to that discussed above for N621. The main difference between the spectra of the two complexes is a general red-shift of all the main spectral features of the N719 with respect to those of the N621 dye. Indeed, the almost equally intense bands I and II are found at 2.35 and 3.22 eV, vs 2.41 and 3.32 eV for N621. Moreover, in the N719 spectrum the intense band III, at 3.97 eV, appears as a single feature, as opposed to the N621 case. As it can be noticed from Figure 9a−c the calculated spectra for the **a**−**c** [N3(2H−2Na)]$^{(0)}$ isomers qualitatively agree with the experimental spectrum, even though for the **c** isomer there is a considerable blue-shift of the absorption maximum of band I with respect to both the **a** and **b** isomers and the experimental spectrum.

Overall, the calculated spectrum of the **b** isomer is the one which seems to better fit the experimental N719 spectrum. However, on the basis of the absorption spectra, it is difficult to make any definitive conclusion about the species effectively present in solution, also considering that all the three isomers have comparable solution free energies (within 0.3 kcal mol^{-1}). If we admit that all the three **a**−**c** isomers are present at the same time in solution, then the resulting spectrum should be a superposition of the spectra computed for the three isomers. By averaging the spectra of the three **a**−**c** [N3(2H−2Na)]$^{(0)}$ isomers (with the assumption that they have all the same concentration in solution), the spectrum in Figure 9d is obtained, which shows an improved agreement with the experiment than the calculated spectra for the single isomers. We notice, however, that the ^{1}H NMR spectra of the N719 complex is not compatible with the presence of the **c** isomer in CD_3OD solution.

A detailed assignment of the transitions composing the spectrum of the **a**−**c** [N3(2H−2Na)]$^{(0)}$ isomers is reported as Supporting Information. The transitions composing band I arise from the first three HOMOs to the pair of LUMO/LUMO+1 states. Therefore, band I is assigned to have a mixed metal-NCS to ligand charge transfer character as in N621, but the excited states are in this case mainly localized on the pyridines

bearing the protonated carboxylic groups. As in the N621 case, for the **a**−**c** $[N3(2H-2Na)]^{(0)}$ isomers band II is composed by a series of transitions spanning the range 2.7−3.7 eV. For all of these transitions, the starting orbitals are the seven HOMOs and the final states involve the entire set of the first six LUMOs. Band II shows also a LL′CT component shifted at lower energy compared to the N621 case. Band III is assigned to have a bipyridine $\pi \rightarrow \pi^*$ character. A summary of the calculated and experimental spectral data in terms of band positions and relative intensities for the N621 and N719 complexes is reported as Supporting Information. For the $[N3(2H-2Na)]^{(0)}$ model, the two lowest singlet−triplet transitions are calculated at 1.77 and 1.82 eV, corresponding essentially to HOMO-1/HOMO → LUMO excitations. Analogously to the lowest singlet excited states, these two transitions give rise to Ru−NCS → dcbpy excited states localized on the pyridines bearing the protonated carboxylic groups (A−A′).

3.5. Lineup of Molecular Energy Levels and TiO_2 Semiconductor Band Edges. A detailed microscopic understanding of the differences in the photovoltaic efficiencies of the different dyes is a very complex issue involving the coupling of the molecule to the semiconductor surface. A number of theoretical studies of organic dyes interacting with TiO_2 surfaces or nanoparticles have been reported.[46] Moreover, Persson recently reported TDDFT calculations on the adsorption of the tetraprotonated form of N3 ($[N3(4H-0Na)]^{(0)}$) on a TiO_2 nanocrystal.[47] While an analogous study for the series of Ru(II)-polypyridyl dyes described in this paper is beyond the scope of the present investigation, it seems interesting to consider how the molecular levels of the different dyes lineup with the band edges of a model TiO_2 nanoparticle. For the latter, we use a $Ti_{38}O_{76}$ cluster of nanometric dimensions, exposing (101) anatase surfaces,[42] see Supporting Information, similar to that employed in refs 46b and 47. Thus, in Figure 10a,b we report the energy levels and the lowest singlet−singlet and singlet−triplet TDDFT excitation energies of the various N3- and N621-derived dyes, respectively, and of the TiO_2 nanoparticle model. For the sake of comparison, we refer to homogeneous data for the dyes and the TiO_2 nanoparticle model, obtained in water solution at the B3LYP/3-21G* level. We point out, however, that qualitatively similar results for the electronic structures of $[N3(2H-2Na)]^{(0)}$ and $[N621(2H-2Na)]^{(0)}$ dyes are obtained using the 3-21G* basis set in water and the larger DGDZVP basis set in ethanol (Figure 6).

For the bare $Ti_{38}O_{76}$ cluster the HOMO and LUMO energies are calculated at −6.55 and −2.77 eV, respectively, resulting in a HOMO−LUMO gap of 3.78 eV. Using TDDFT, the lowest transition is reduced to 3.20 eV, a value only slightly smaller than typical band gaps of TiO_2 nanoparticles of a few nm size.[44] As it can be noticed from Figure 10a,b for all the investigated dyes, the orbital set formed by the seven dye HOMOs fall within the TiO_2 gap.

The $[N3(4H-0Na)]^{(0)}$complex, which corresponds to the N3 dye with four protonated carboxylic groups, is the species which shows the smallest HOMO−LUMO gap and the lowest first singlet−singlet and singlet−triplet excitation energies among the considered dyes, 2.58, 1.88, and 1.69 eV, respectively. Moreover, the LUMO of this species is found to lie slightly below (0.03 eV) the energy of the TiO_2 conduction band. Moving to the $[N3(2H-2Na)]^{(0)}$ model of the N719 dye, the LUMO energy raises by only 0.17 eV, so that it lies slightly above the energy of the TiO_2 edge. The increased HOMO−LUMO gap and first excitation energies (2.67, 1.97, and 1.76 eV, respectively) with respect to $[N3(4H-0Na)]^{(0)}$ are due essentially to the LUMO destabilization. It is also interesting to compare the results obtained for the $[N3(2H-2Na)]^{(0)}$ with those for the corresponding $[N3(2H-0Na)]^{(2-)}$ anionic complex, in which no counterions are present. As it can be noticed from Figure 10a, both the occupied and unoccupied levels of $[N3(2H-0Na)]^{(2-)}$ are raised in energy with respect to those of $[N3(2H-2Na)]^{(0)}$, while comparable HOMO−LUMO gaps and first excitation energies are found in the two cases, with the LUMO of the anionic complex being 0.28 eV above the TiO_2 conduction edge. For all the monoprotonated species the electronic structures of the **a′** and **b′** isomers do not show significant differences, so that only results obtained for the **a′** isomers will be discussed. For $[N3(1H-3Na)]^{(0)}$ the occupied and unoccupied orbitals are only slightly higher in energy with respect to the diprotonated $[N3(2H-2Na)]^{(0)}$ complex; the computed HOMO−LUMO gaps and first excitation energies are similar for the two species, and also the alignment of the LUMO energy with the TiO_2 conduction band edge is similar. Also for the monoprotonated species, removing the Na^+ counterions raises the energy of both the occupied and unoccupied orbitals by a similar amount, thus resulting in a HOMO−LUMO gap and first excitation energy similar to those of the corresponding diprotonated complex. The LUMOs of the tetradeprotonated $[N3(0H-4Na)]^{(0)}$ and $[N3(0H-0Na)]^{(4-)}$ species lie at still higher energy, and are found 0.44 and 0.92 eV above the edge of the TiO_2 conduction band. Again, the effect of the counterions is to downshift the energies of both the occupied and unoccupied orbitals. In the case of the anionic complex, however, the shift of the unoccupied orbitals is considerably larger than that of the occupied ones, with a consequent increased HOMO−LUMO gap and lowest excitation energies. This shift of the unoccupied orbitals is related to the increased electron density on the deprotonated carboxylic groups which raises the energy of the bipyridine π^* orbitals and results in an increase of the HOMO−LUMO gap and of the first excitation energy compared to the partially and fully protonated complexes.[40e] This behavior is responsible of the relevant alochromic effect observed in the N3 dye upon increasing the pH, [40e,45] which translates into a blue-shift of the main spectral features increasing the pH from 1 (where all four carboxylic groups are protonated) to 9 (where the carboxylic groups are all deprotonated).[45] On the technical side, we notice that inclusion of 8 water molecules explicitly solvating the carboxylates of $[N3(0H-0Na)]^{(4-)}$, leads to small changes in the HOMO−LUMO gap and lowest singlet−singlet and singlet

(44) (a) Yang, M.; Thompson, D. W.; Meyer, G. J. *Inorg. Chem.* **2000**, *39*, 3738−3739. (b) Weng, Y. X.; Wang, Y. Q.; Asbury, J. B.; Ghosh, H. N.; Lian, T. *J. Phys. Chem. B* **2000**, *104*, 93−104. (c) Yang, M.; Thompson, D. W.; Meyer, G. J. *Inorg. Chem.* **2002**, *41*, 1254−1262. (d) Khoudiakov, M.; Parise, A. R.; Brunschwig, B. S. *J. Am. Chem. Soc.* **2003**, *125*, 4637−4642.
(45) Nazeeruddin, M. K.; Zakeeruddin, S. M.; Humpry-Baker, R.; Jirousek, M.; Liska, P.; Vlachopoulos, N.; Shklover, V.; Fisher, C.-H.; Grätzel, M. *Inorg. Chem.* **1999**, *38*, 6298−6305.
(46) (a) Vittadini, A.; Selloni, A.; Rotzinger, F. P.; Gratzel, M. *J. Phys. Chem. B* **2000**, *104*, 1300−1306. (b) Persson, P.; Bergstrom, R.; Lunell, S. *J. Phys. Chem. B* **2000**, *104*, 10348−10351. (c) Stier, W.; Prezhdo, O. V. J. *Phys. Chem. B* **2002**, *106*, 8047−8054. (d) Rego, L. G. C.; Batista, V. S. *J. Am Chem. Soc.* **2003**, *125*, 7989−7997. (e) Stier, W.; Duncan, W. R.; Prezhdo, O. *Adv. Mater.* **2004**, *16*, 240−244. (f) Duncan, W. R.; Stier, W. M.; Prezhdo, O. *J. Am. Chem. Soc.* **2005**, *127*, 7941−7951.
(47) Persson, P.; Lundqvist, M. J. *J. Phys. Chem. B*, **2005**, *109*, 11918−11924.

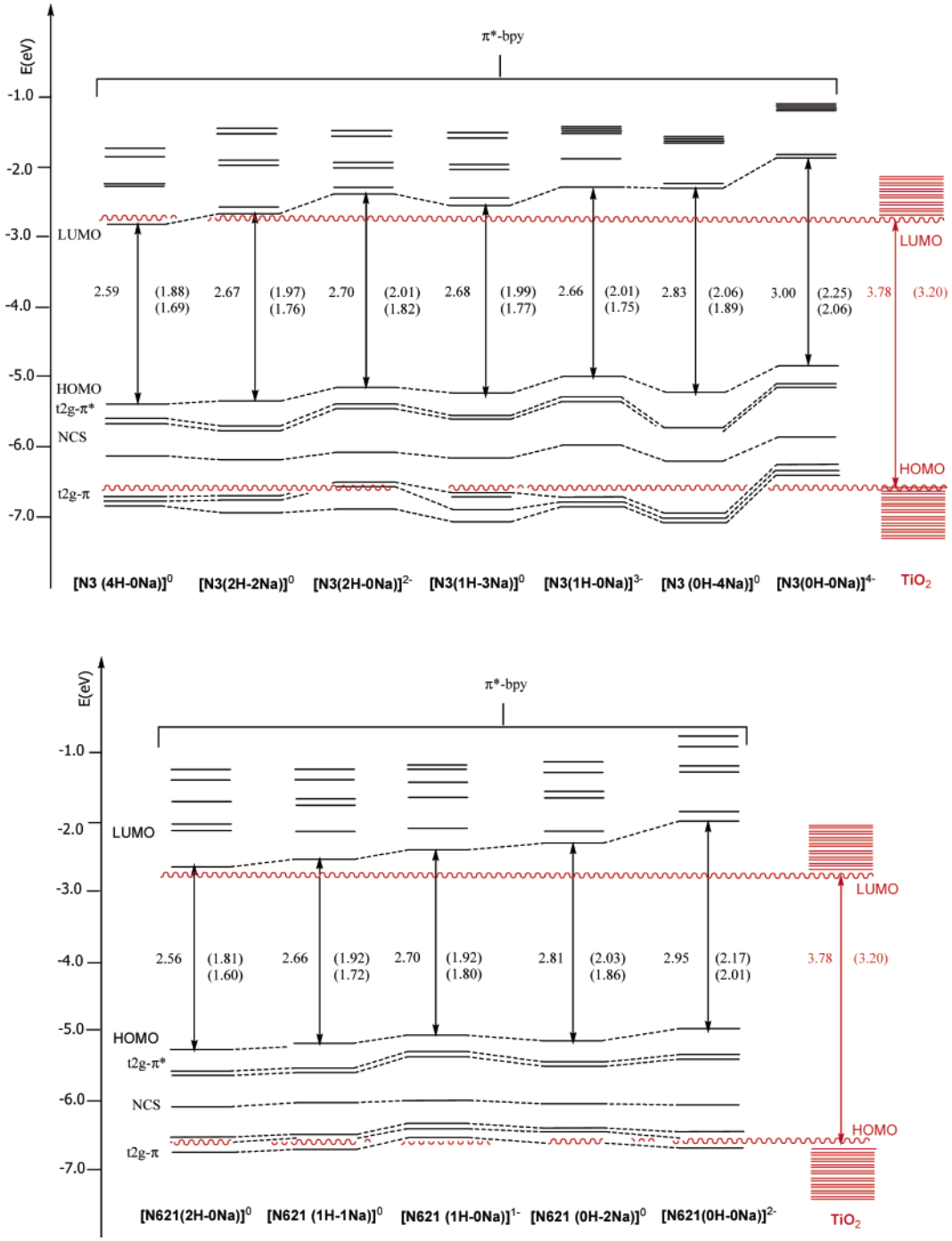

Figure 10. Energy levels and lowest TDDFT singlet−singlet and singlet−triplet excitation energies (data in parentheses, first and second entries, respectively) calculated at the B3LYP/3-21 g* level in water solution for the various dyes originated from the N3 (upper panel) and N621 (lower panel) complexes, compared to results for a model of a TiO_2 nanoparticle.[42] The edges of the TiO_2 valence and conduction band are represented as red discontinuous lines. For the diprotonated N3-derived dyes, data relative to the **a** isomer have been reported. For the monoprotonated N3- and N621-derived dyes, data relative to the **a′** isomers have been reported. The bipyridine π bonding orbitals and the COO^- oxygen lone pairs are omitted for clarity.

triplet excitation energies with respect to results obtained by simply embedding $[N3(0H-0Na)]^{(4-)}$ in a polarizable continuum solvation model (2.88 vs 3.00, 2.12 vs 2.25 and 1.94 vs 2.06 eV, respectively). Also, the absolute HOMO and LUMO energies are both downshifted with respect to the case in which explicit solvation is not considered (−5.01 vs −4.86 and −2.13 vs −1.85 eV, respectively). These changes, however, do not qualitatively alter the alignment of the dye and TiO_2 energy levels and are expected to be even smaller for the neutral species and for the anionic species containing a larger number of protons, suggesting that a continuum model of solvation is a good approximation for the prediction of the optical properties of Ru(II)-polypyridyl dyes.

Even though our calculations do not include the coupling of the Ru-polypyridyl dye to the TiO_2 nanoparticle, we can use the calculated data to speculate which of the investigated complexes should be the best sensitizer for TiO_2. On the basis of the present calculations, the di- and monoprotonated ($[N3-(2H-2Na)]^{(0)}$ and $([N3(1H-3Na)]^{(0)}$) models of the N719 dye seem to represent an optimal choice with respect to the fully

protonated and fully deprotonated species, since these dyes show a good light-harvesting capability (as reflected by the relatively small first singlet−singlet excitation energies of 1.97 and 1.99 eV, respectively) coupled to an almost perfect alignment of their excited states with respect to the TiO_2 conduction band edge. Indeed, while the fully protonated N3 species has an excellent light-harvesting capability (low HOMO−LUMO gap and first singlet−singlet excitation energy) the fact that the LUMO lies slightly below the edge of the TiO_2 conduction band might imply that not all the absorbed light could be used for electron injection. Moreover, as reported experimentally, adsorption of the tetra-protonated carboxylic groups leads to a decreased open-circuit potential.[10] An almost exactly opposite situation is encountered for the fully deprotonated species, for which the lowest unoccupied orbitals are calculated to lie well above the TiO_2 conduction band edge; however, the light-harvesting capability of this species in the low-energy spectral range is expected to be inferior to that of the fully protonated N3 species.

It is interesting to point out that for the alizarin-TiO_2 system,[46e−f] non adiabatic molecular dynamics simulations have shown that efficient electron injection from a dye excited-state lying below the TiO_2 edge to the TiO_2 conduction band can effectively take place, due to fluctuations in the dye excited-state energy related to the nuclear dynamics.[46e−f] These results might be relevant to explain the high photocurrent generated in dye-sensitized solar cell devices employing the tetra-protonated $[N3(4H-0Na)]^{(0)}$ species,[10] for which we calculate a slightly unfavorable alignment of dye excited states with the TiO_2 conduction band edge. Remarkably, our results obtained considering the noninteracting dyes and nanoparticle are in qualitative agreement with the electronic structure of the $[N3(4H-0Na)]^{(0)}/TiO_2$ system reported by Persson,[47] showing for this system two dye LUMOs lying below the first TiO_2 unoccupied state.

For the N621-derived dyes we calculate similar variations of the electronic structure as a function of protonation and counterions as for the N3-derived dyes, see Figure 10. However, for the N621-derived dyes the most favorable situation is calculated for the diprotonated $[N621(2H-0Na)]^{(0)}$ dye, which shows an almost perfect alignment of the LUMO with the edge of the TiO_2 conduction band, coupled to a good light-harvesting capability. The monoprotonated and fully deprotonated $[N621-(1H-1Na)]^{(0)}$ and $[N621(0H-2Na)]^{(0)}$ species show an increased HOMO−LUMO gap and first excitation energy with respect to the diprotonated dye, due to a different destabilization of the energy of the occupied and unoccupied states. Such raising of the unoccupied orbitals energy results in a reduced light-harvesting capability of these dyes.

The computed electronic structure changes discussed above are consistent with the photovoltaic data for the mono- and diprotonated N719 complexes. Indeed, the electronic structure of the two species is rather similar, despite the different number of protons. In particular, both species show a similar alignment of the LUMOs with the TiO_2 conduction band edge, coupled to a comparable light-harvesting capability, so that they should provide comparable excited-state electron injection efficiencies. This is in agreement with the similar photocurrents observed with the diprotonated and monoprotonated N719 species. The increased overall potential obtained with the monoprotonated species, due to the upshift of the Fermi level of the system, is not associated to a significant reduction of the photocurrent, thus leading to an increased overall efficiency.

The slightly reduced overall efficiency of the diprotonated N621 dye with respect to the corresponding N719 species might then arise because of the different possible adsorption geometries of the two dyes on the TiO_2 surface. The N621 dye will be forced to adsorb on the semiconductor surface using either a single carboxylic group or two carboxylic groups residing on the same bipyridine, while the N719 dyes might use carboxylic groups bound to two different bipyridines.

4. Summary and Conclusions

In this paper, we have presented a combined experimental and theoretical study of ruthenium(II)-polypyridyl sensitizers for solar cell devices, derived from the $[Ru(dcbpyH_2)_2(NCS)_2]$, N3, and $[Ru(dcbpyH_2)(tdbpy)(NCS)_2]$, N621, ($dcbpyH_2$ = 4,4′-dicarboxy-2,2′-bipyridine, tdbpy = 4,4′-tridecyl-2,2′-bipyridine) complexes. On the experimental side, a purification procedure was developed to obtain pure N-bonded isomers of both types of sensitizers. The effect of dye protonation on the photovoltaic properties of the two types of dyes was investigated. Employing a swift self-assembling deposition procedure, we have obtained for the N719 and N621 diprotonated complexes 10.26 and 9.57% solar cell efficiency, respectively, under 1 sun. The photovoltaic data of the purified N719 sensitizer adsorbed on TiO_2 films in its monoprotonated state, exhibited a remarkable 11.18% power conversion efficiency at 1 sun, the increased performance with respect to the diprotonated dye being essentially related to an increased cell voltage.

To gain a better understanding of the role of the sensitizer, particularly of its electronic structure and excited-state properties in the efficiency of dye-sensitized solar cell devices, we have carried out Density Functional Theory (DFT) and Time Dependent DFT (TDDFT) calculations in solution of the geometry, electronic structure and optical absorption spectra of a complete series of sensitizers derived from the N3 and N621 complexes.

The calculated electronic structure in terms of molecular orbital energies and localization is consistent with the experimental redox potentials. In particular, the cathodic shift in the oxidation potential of the N719 species compared to N621 is reproduced by our calculations, as well as the presence of two separate reduction potentials for the N621 complex, which we assign to reduction of the bipyridine ligands bearing the carboxylic and alkyl substituents, respectively.

The good agreement between the experimental and the TDDFT calculated absorption spectra of the N3- and N621-derived sensitizers allowed us to provide a detailed assignment of the main spectral features of the investigated dyes. In particular, the two bands at 2.3−2.4 eV and 3.2−3.3 eV in the nonprotonated and diprotonated N621 and N719 spectra are assigned to as mixed metal-thiocyanate to bipyridine charge-transfer transitions. Interestingly, the bands found at 3.2−3.3 eV in the spectra of both complexes also show a contribution arising from a ligand (NCS) to ligand (bipyridine) charge-transfer transition and from weak d−d excitations. At higher energies, the intraligand $\pi-\pi^*$ transitions of the bipyridine ligands are found. For the N621-derived complex two types of $\pi-\pi^*$ transitions are calculated, corresponding to excitations within the bipyridine ligand bearing the carboxylic and alkyl substituents in the para positions.

From the present extensive study, we can infer some general trends concerning the effect of protonation and counterions on the electronic structure and optical properties of the investigated dyes. In particular, deprotonation of the terminal carboxylic groups causes a different destabilization of the occupied and unoccupied orbitals, which ultimately leads to increased HOMO−LUMO gaps and excitation energies with increasing deprotonation. In both the N3- and N621-derived dyes the fully protonated and fully deprotonated species show the smallest and largest, respectively, HOMO−LUMO gap and first excitation energies. This effect is related to the increased electron density on the deprotonated carboxylic groups which raises the energy of the bipyridine π^* orbitals.

We finally compared how the molecular orbitals of the different complexes investigated in this paper lineup with the band edges of a model TiO_2 nanoparticle consisting of a $Ti_{38}O_{76}$ cluster exposing anatase (101) surfaces. Based on this analysis, we suggest that the di- and monoprotonated forms of the N3-derived dyes represent an optimal choice with respect to the fully protonated and deprotonated species because of the good compromise between their light-harvesting capability and the alignment of their excited states with the TiO_2 conduction edge. Indeed, the fully protonated N3 species has an excellent light-harvesting capability but the lowest unoccupied orbital lies slightly below the edge of the TiO_2 conduction band, so that not all the absorbed light could be used for charge injection, while in the fully deprotonated N3 dye all the unoccupied orbitals lie well above the TiO_2 conduction edge, but its limited response in the red region of the spectrum reduces its light-harvesting capability. Similar characteristics are shown by the amphiphilic heteroleptic sensitizer N621, for which the diprotonated species seems to represent an optimal choice. The improved stability toward water-induced desorption from TiO_2 of the N621-derived sensitizers renders them attracting candidates for the generation of water-stable solar cell devices.

We finally remark that the present results have been obtained considering the noninteracting dye and semiconductor systems. A detailed theoretical study on the role of protonation in the interacting dye-semiconductor systems is in progress.

Acknowledgment. We acknowledge financial support of this work by the Swiss Science Foundation, Swiss Federal Office for Energy (OFEN), U. S. Air Force Research Office under Contract No. F61775-00-C0003, and the Institute for Applied Photovoltaics (INAP, Gelsenkirchen, Germany). We thank Dr. S. M. Zakeeruddin, Davide Di Censo, Claudia Barolo, Dr. Robin Humphry-Baker and Pascal Comte for their kind assistance. Guido Viscardi was supported by the University of Torino and is particularly grateful to Compagnia di San Paolo (Torino) and Fondazione della Cassa di Risparmio di Torino (Italy), for the supply of laboratory equipment.

Supporting Information Available: Experimental section (Materials, Analytical measurements, photovoltaic measurements Purification on Sephadex LH-20). Theoretical section (Excitation energies, oscillator strength (*f*) and composition of the TDDFT eigenvectors for the $[N621(0H-2Na)]^{(0)}$ and $[N3(2H-2Na)]^{(0)}$ dyes. Simulation of the $[N621(0H-2Na)]^{(0)}$ spectrum in ethanol by a variable σ. Optimized structure of the TiO_2 nanoparticle model. Full ref 33.) This material is available free of charge via the Internet at http://www.pubs.acs.org.

JA052467L